# Determination of the structural, electronic, and optical properties of the $CH_3NH_3SiCl_3$ perovskite using an ab initio method.

**Résumé** :

In this study, the structural, electronic and optical properties of the perovskite $CH_3NH_3SiCl_3$ were investigated using DFT. A kinetic cutoff energy of 80 Ry and Monkhorst-Pack k-points of 10×10×10 were used. The lattice constant obtained is 5.72 Å. The material exhibits a direct bandgap of 2.509 eV along the R–R path in the Brillouin zone. The valence band is characterised by the 2p states of Cl, C and N, whilst the conduction band is characterised by the 2p states of Si. The refractive index is greater than 2 in the infrared but lower in the visible, and decreases further in the ultraviolet. The extinction coefficient K(ω) and the absorption coefficient show the same trend. In the infrared and visible regions, K(ω) is greater than 1, but in the ultraviolet, it is less than 1.The extinction coefficient K(ω) shows that there is no attenuation of incident light between 7 eV and 8 eV, and between 10.8 eV and 20 eV. The reflectance suggests that the material can reflect light from 0 to 7.5 eV and then from 8 eV to 12 eV. Absorption therefore occurs in the infrared and visible regions. Optical conductivity is present in the IR and visible regions but is practically zero in the ultraviolet. The electron energy loss function L(ω) exhibits a maximum peak at 16.41–10.521 eV, corresponding to the material's plasma frequency. At this maximum peak, the electrons begin to vibrate in unison under the influence of light. These results reveal that $CH_3NH_3SiCl_3$ can be used in electronic and optoelectronic devices and other technologies. Several avenues of research are opening up, such as the exploitation of optical and electronic properties in the infrared, visible and ultraviolet regions, and applications in photovoltaic cells.

**Keywords**: $CH_3NH_3SiCl_3$ perovskites, DFT, Structural properties, Electronic properties, Optical properties.

## INTRODUCTION

The current energy crisis calls for a significant shift in energy sources that takes environmental protection into account. The environment has been considerably degraded in recent years as a result of the increased exploitation of conventional energy sources [1]. Renewable energies are the leading contenders. Numerous studies have shown that photovoltaic energy could meet current energy needs. This sector is still dominated by silicon, CdTe, CIGS, GaAs and others, the extraction of which has a detrimental impact on the environment [2,3,4,5]. To achieve this energy transition, we must therefore turn to other materials. Perovskites possess very interesting properties and could replace these currently used materials. Studies carried out in 2015 reported perovskite solar cells with an efficiency of 20 per cent, which is close to the 25 per cent efficiency of silicon cells [6,7].Hybrid organic

UNDER PEER REVIEW IN IJAR

perovskites are the most widely studied. They possess exceptional optoelectronic properties: high light absorption, excellent charge mobility and an adjustable bandgap [8,9,10]. They are easy to manufacture: low-temperature synthesis, ink-based deposition – and they are cost-effective. They utilise inexpensive techniques such as spin-coating, spraying or industrial printing, and are compatible with plastics. Several applications stand out for these materials: solar cells, lighting and displays (LEDs), luminescence capabilities, sensors and detectors [11,12,13]. The most widely studied organic hybrid perovskite is lead methylammonium triiodide ($CH_3NH_3PbI_3$) or MAPI. Studies have shown a bandgap between 1.55 eV and 1.66 eV, with interesting optical and electronic properties, such as: a high absorption coefficient and high electron and hole mobility in this material [14,15].The efficiency of MAPI-based solar cells was 3.8 per cent in 2009 [16] and 25.03 per cent in 2023 [17], whilst others even predict 31 per cent [18]. The perovskite $CH_3NH_3PbI_3$ is a promising material for the photovoltaic sector, given current technologies, etc. However, this perovskite contains the element lead (Pb), which is known for its toxicity [19]. The environment, and indeed humans, may be exposed to it. This is why, in our approach, we are focusing instead on the perovskite of the methylammonium trichlorosilicate type, $CH_3NH_3SiCl_3$ or MASiCl. In this work, we have investigated the structural, electronic and optical properties of the cubic perovskite material methylammonium silicitrichloride ($CH_3NH_3SiCl_3$) using density functional theory with the PBE-GGA functional. To the best of our knowledge, there are no data available on the electronic and optical properties of $CH_3NH_3SiCl_3$. However, Lhouceine Moulaoui et al. have studied the perovskites $CH_3NH_3PbCl_3$ and $CH_3NH_3PbBr_3$ in their work [20]. Grover, K. et al. also studied the cubic Pm-3m-type $CH_3NH_3PbCl_3$ [21]. Caputo, M. et al. focused instead on $CH_3NH_3PbCl_3$[22]. The results obtained by these authors are highly significant. In our approach, we substituted silicon for lead to investigate the likely properties. The results obtained pave the way for the use of this material in new technologies.

## 2. Computational Details

In this work, we used the Quantum ESPRESSO code, which is based on Density Functional Theory (DFT) [22, 23, 24]. We evaluated the total energies, structural properties, electronic properties and optical properties of the $CH_3NH_3SiCl_3$ perovskite. To this end, we optimised the geometry using a relaxation calculation. The exchange-correlation potential used was the Perdew–Burke–Ernzerhof generalised gradient approximation (PBE + GGA) [25, 26]. The methylammonium trichlorosilicate perovskite $CH_3NH_3SiCl_3$ is assumed to crystallise in the Pm-3m cubic structure. Figure 1 shows a crystal structure representation of this compound.

UNDER PEER REVIEW IN IJAR

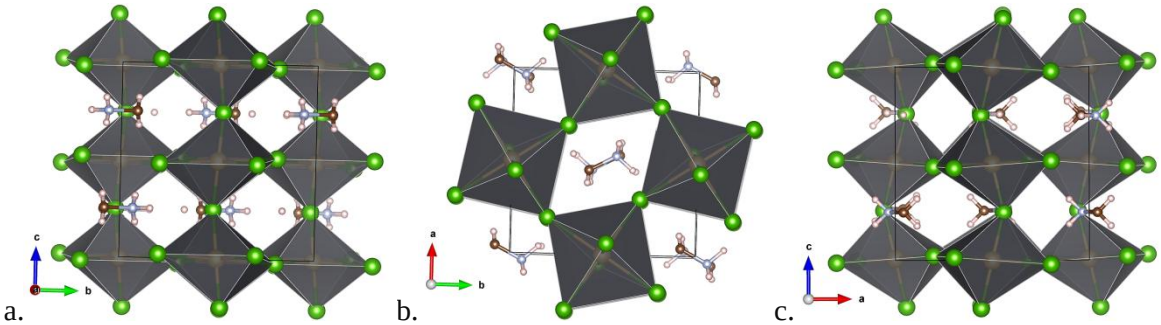



Figure 1. Structure of $CH_3NH_3SiCl_3$ along (a) (100), (b) (001) (b) and (c) (010).

The total energy tolerance was set at $10^{-9}$ eV. The kinetic energy cut-off (Ecutoff) was set at 80 Ry. We performed an integration of the Brillouin zone [27] using a Monkhorst grid [27] with dimensions of 10 × 10 × 10 for perovskite structures. The path followed within the Brillouin zone is X–Γ–M–X–R–Γ.

## 3. RESULTS AND DISCUSSION

### 3.1. Convergence test.

To perform a DFT calculation, a relaxation-based convergence calculation is used to obtain optimal values for the calculation parameters. The parameters that are relaxed or optimised are: the mesh parameter, the kinetic energy cut-off, and the Monkhorst-Pack k-points.

***Lattice parameter***

Figure 2 shows how the total energy of the system varies with the lattice parameter. The lattice parameter at equilibrium corresponds to the lowest energy value. The lattice parameter obtained is 5.72 Å.

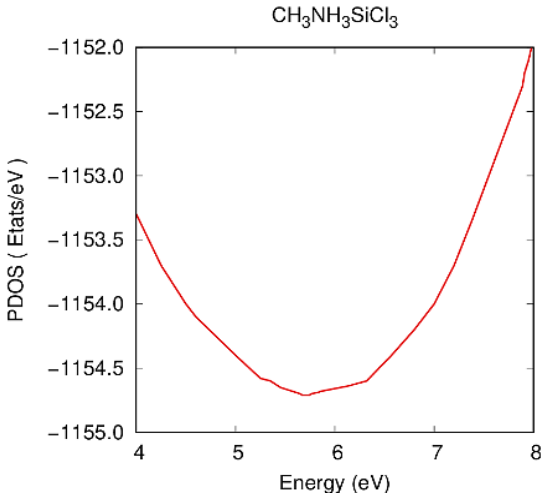



Figure 2. Convergence of Lattice Parameter of $CH_3NH_3SiCl_3$perovskite.

***Convergence of Kinetic energy cut-off***

La figure 3 présente la convergence de l'énergie cinétique de coupure. La coupure d'énergie cinétique ($E_{cut}$) indique que seules les ondes planes avec une énergie cinétique inférieure au seuil de $E_{cut}$ sont prises en compte par le calcul.Comme on ne peut pas inclure une infinité d'ondes planes dans les

UNDER PEER REVIEW IN IJAR

calculs, celles de plus haute énergie sont éliminées. Plus l'énergie cinétique de coupure est élevée, plus la représentation des électrons autour des noyaux est précise, alors plus la grille spatiale doit être fine, ce qui sature la mémoire et rallonge le temps de calcul. Pour trouver le meilleur choix, on réalise un test de convergence. Sous Quantum ESPRESSO, cela consiste à optimiser ecutwfc (pour les fonctions d'onde) et ecutrho (pour la densité de charge), la valeur de cette dernière étant généralement 4 à 8 fois plus élevée que la première. La DFT repose sur l'équation de Kohn-Sham [28]. Cette équation s'écrit:

Figure 3 shows the convergence of the kinetic energy cut-off. The kinetic energy cut-off ($E_{cut}$) indicates that only plane waves with kinetic energy below the $E_{cut}$ threshold are taken into account in the calculation. As it is not possible to include an infinite number of plane waves in the calculations, those with higher energy are eliminated. The higher the kinetic energy cut-off, the more accurate the representation of electrons around the nuclei, and therefore the finer the spatial grid must be; this places a heavy load on memory and increases the computation time. To determine the optimal choice, a convergence test is carried out. In Quantum ESPRESSO, this involves optimising ecutwfc (for the wavefunctions) and ecutrho (for the charge density), the value of the latter generally being 4 to 8 times higher than the former. DFT is based on the Kohn–Sham equation [28]. This equation is written as:

$$\left[-\frac{\hbar^2}{2m_e}\nabla^2 + V_{eff}(r)\right]\psi_{nk}(r) = \varepsilon_{nk}\psi_{nk}(r) \quad \#(1)$$

$\psi_{nk}(r)$is the electron wave function, $\varepsilon_{nk}$ :the electron's rest energy, $n$ : the band index, $\vec{k}$ : wave vector in the first Brillouin zone and$V_{eff}$ :the Kohn-Sham effective potential. Wave functions$\psi_{nk}(r)$are expanded in terms of plane waves of the form:

$$\psi_{nk}(r) = \frac{1}{\sqrt{\Omega}}\sum_{G} C_{n,\vec{k}+\vec{G}} e^{i(\vec{k}+\vec{G}).\vec{r}} \#(2)$$

The kinetic energy associated with such a plane wave is given by:

$$E_{cin}(\vec{k}) = \frac{\hbar^2}{2m}(\vec{k}+\vec{G})^2 \#(3)$$

The cutting-off kinetic energy is derived from this function. The parameter `ecutwfc` sets the cutting-off energy that limits the size of the plane wave basis used to expand the electron wave functions. The condition for selecting this is:

$$\frac{\hbar^2}{2m}(\vec{k}+\vec{G})^2 \leq E_{cut}^{wfc} \#(4)$$

The convergence test yields a cutoff kinetic energy (Ecutoff) of 80 Ry.

The Monkhorst-Pack grid [27] that we used consists of $10 \times 10 \times 10$points to sample the k-points in the Brillouin zone. This grid is suitable for achieving very high accuracy in this study.

UNDER PEER REVIEW IN IJAR

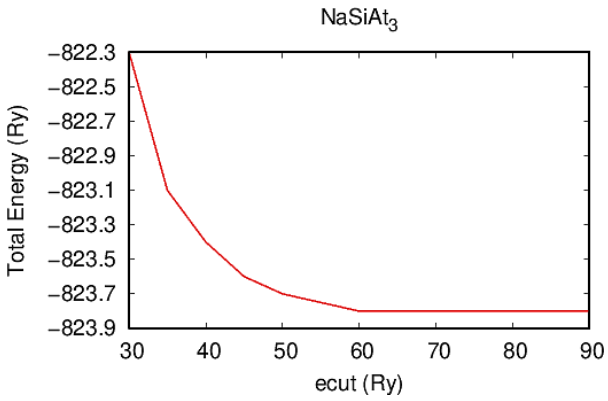



Figure 3. Convergence of Kinetic energy cut-off ecut of $CH_3NH_3SiCl_3$perovskite.

***Path in the Brillouin zoneand Monkhorst grid of points***

Figure 4 shows the path followed in the Brillouin zone. The first Brillouin zone corresponds to the unit cell of the reciprocal lattice [27]. It is constructed using the medians of the direct lattice vectors between nearest neighbours. The path followed in the Brillouin zone is X-Γ-M-X-R-Γ.

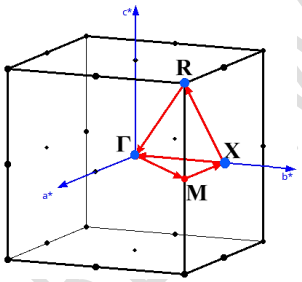



Figure 4. X-Γ-M-X-R-Γ path in the Brillouin zone.

### 3.2. Electronic properties

The results obtained for the electronic properties are: the band structure, the total density of states (TDOS), the partial densities of states (PDOS) and the charge density.

#### 3.2.1. Electronic band structure and gap

The electronic properties obtained are: the electronic band structure, the energy gap, the partial state densities and the total state density. The band structure provides information on the magnetic, electronic, optical and thermal properties of a material [15, 29]. It is obtained by solving the Kohn–Sham equation [28], i.e. equation (1). The desired result is given by the dispersion relation:

$$E_n = E_n(\vec{k}) \#(5)$$

The dispersion can be approximated by a parabola when one is close to a band extremum:

$$E_n(\vec{k}) = E_n(\vec{k}_0) + \frac{\hbar^2}{2m_e}\left|\vec{k} - \vec{k}_0\right|^2 \quad \#(6)$$

This last relationship can simply be written as :

UNDER PEER REVIEW IN IJAR

$$E(k) = \frac{\hbar^2 k^2}{2m} \quad \#(7)$$

The electronic band structure is the representation of $E_n(\vec{k})$ as a function of $\vec{k}$. It describes the allowed energy levels and the forbidden energy levels. Three regions are particularly important: the valence band, the conduction band and the band gap. The valence band is the highest energy band occupied by electrons at low temperature. The conduction band, situated above the valence band (which is often empty), facilitates the free movement of conduction electrons. The band gap is the energy interval between these two bands in which no electronic states are permitted. The nature of the material depends on the width of the band gap. The electronic band structure along the path X–Γ–M–X–R–Γ in the first Brillouin zone is shown in Figure 4.

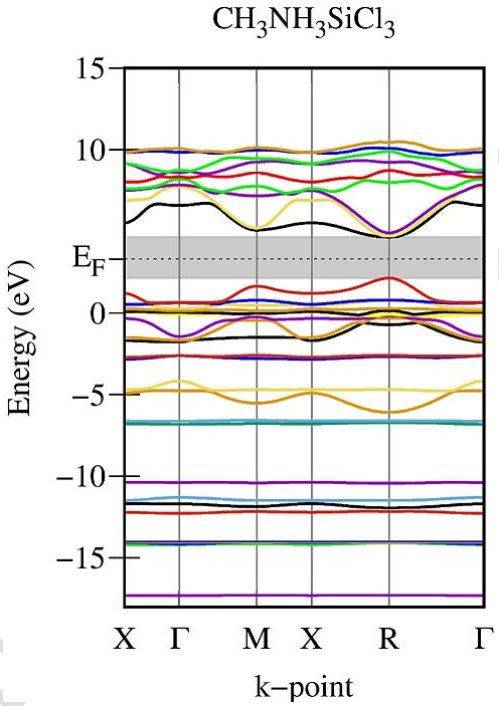



Figure 4 : Electronic band structure of $CH_3NH_3SiCl_3$.

The band gap of the $CH_3NH_3SiCl_3$ perovskite material studied is 2.509 eV. As this band gap is small, the material can be considered a semiconductor. Lhouceine Moulaoui et al, in their study, obtained band gaps of 2.402 eV and 2.415 eV for $CH_3NH_3PbCl_3$ and $CH_3NH_3PbBr_3$ respectively [20]. Grover, K. et al, on the other hand, obtained a bandgap of 2.90 eV for the cubic Pm-3m-type perovskite $CH_3NH_3PbCl_3$ [21]. Caputo, M. et al also obtained a bandgap of 2.90 eV for $CH_3NH_3PbCl_3$ [22]. Comparing our result with those of Grover, K. et al. and Caputo, M. et al., the band gap appears to decrease when Si is substituted for Pb. The band gap obtained in our work is direct in the R–R path direction. Kolomiiets et al. obtained a bandgap value of 2.53 eV for GGA-PBEsol without SOC and 1.33 eV for GGA-PBEsol with SOC for the perovskite $CH_3NH_3PbCl_3$ [30]. Their results merely confirm ours.

### 3.2.1. Partial and total densities of state

***Density of States calculation***

UNDER P IN IJAR

According to band theory, electrons cannot occupy any continuous energy level. In reality, they are confined to eigenstates of the wave vector $\vec{k}$. The density of states g(E) for a volume V is given by the relation :

$$g(E) = \frac{1}{V}\sum_{n,\vec{k}} \delta\left[E - E_n(\vec{k})\right] \#(8)$$

In the reciprocal space, the space of $\vec{k}$, for a particular band, it is written as:

$$g(E) = \frac{g_S}{(2\pi)^d}\int_{iso-énergie\ E} \frac{d\vec{k}}{\left|\nabla_{\vec{k}} E(\vec{k})\right|} \#(9)$$

where $g_S$ is the degeneracy factor. Analysis of the total density of states (TDOS) and partial densities of states (PDOS) provides insight into the contribution of the various atomic orbitals and the nature of the bonds between atoms in the material. The total density of states and partial densities of states for the perovskite $CH_3NH_3SiCl_3$ are shown in Figure 5.

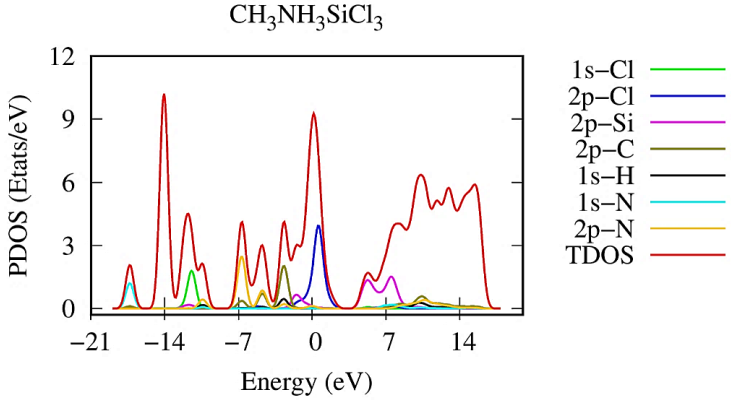



Figure 5 : Calculated total and partial densities of states for $CH_3NH_3SiCl_3$.

We have shown that the electronic band structure has a band gap lying between 2.135 eV and 4.645 eV. The valence band of $CH_3NH_3SiCl_3$ is characterised by the 2p-Cl state. However, it is slightly mixed with the 2p-C, 2p-Si and 2p-N states. The conduction band, on the other hand, is dominated by the 2p-Si state. Let us examine the bandgap boundaries, as illustrated in Figure 6, which shows the bandgap edges of the $CH_3NH_3SiCl_3$ perovskite structure.

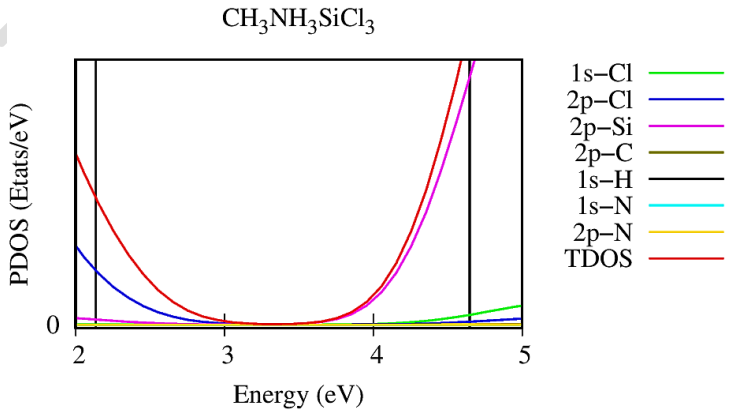



Figure 5 : Atomic orbitals around the band gap of $CH_3NH_3SiCl_3$.

UNDER PEER REVIEW IJAR

Normally, the forbidden band does not allow any states within it. However, on closer inspection, it can be seen that it is overlapped by two states that lie entirely within it. These are the 2p state of Cl and the 2p state of Si, which will have the effect of reducing the value of the band gap.

### 3.3. Optical properties

#### 3.3.1. Real part and imaginary part of the complex dielectric function

To describe the optical properties of a material , one must analyse the complex dielectric function $\tilde{\varepsilon}$. This function is expressed as :

$$\tilde{\varepsilon}(\omega) = \varepsilon_r(\omega) + i\varepsilon_i(\omega) \quad \#(10)$$

$\varepsilon_r(\omega)$ is the real part of the complex dielectric function $\tilde{\varepsilon}$ and $\varepsilon_i(\omega)$ is the imaginary part. The imaginary part $\varepsilon_i(\omega)$ of the dielectric function is expressed as:

$$\varepsilon_i(\omega) = \frac{Ve^2}{2\pi h\omega^2 m^2}\int d^3k \sum |\langle \Psi_C|P|\Psi_V\rangle|^2\, \delta\left(E_C - E_V - \frac{h\omega}{2\pi}\right) \#(11)$$

$\Psi_C$ and $\Psi_V$ are the wave functions of the conduction and valence bands, respectively; $E_C$ and $E_V$ are the energy levels of the conduction and valence bands, respectively. e, h, ω, m and P are the electron charge, Planck's constant, the angular frequency of the incident photon, the mass of the electron and the momentum operator, respectively..

$\varepsilon_r(\omega)$ et $\varepsilon_i(\omega)$are determined using the Kramers–Kronig relations given by::

$$\varepsilon_r(\omega) = 1 + \frac{2}{\pi} P \int_0^{\infty} \frac{\omega' \varepsilon_i(\omega')}{\omega'^2 - \omega^2} d\omega' \quad \#(12)$$

$$\varepsilon_i(\omega) = -\frac{2\omega}{\pi} P \int_0^{\infty} \frac{\varepsilon_r(\omega') - \&}{\omega'^2 - \omega^2} d\omega' \quad \#(13)$$

We have plotted the real and imaginary parts of the complex dielectric function of $CH_3NH_3SiCl_3$ from 0 eV to 20 eV in Figure 9.

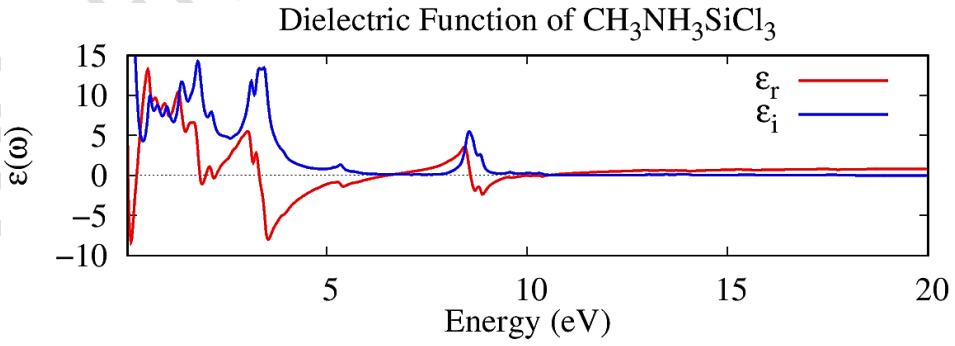



Figure 9 : Real part (in red) and imaginary part (in blue) of the dielectric function calculated.

These two functions are characterised by two distinct regions: from 0 to 10 eV, where they vary with fluctuations, and from 10 to 20 eV, where they cancel each other out. The imaginary part is entirely positive, whilst the real part consists of both positive and negative components.

The real part is divided into three regions: the first region from 0 to 5 eV, the second region from 5 eV to 10 eV and, finally, the third region from 10 eV to 20 eV. In the first region, there are

UNDER PEER REVIEW IN IJAR

several peaks with strong positive and negative fluctuations; in contrast, in the second region, there is only one major peak. The second region is characterised by lower values than the first. The final region shows very low values, very close to zero: the material therefore becomes transparent. The static dielectric constant $\varepsilon_1(0)$ is 2.5. It is known as the limit value of the complex dielectric function $\varepsilon(\omega)$ when the irradiation frequency is close to zero. It should also be noted that $\varepsilon_1$ is negative over the intervals [0.04, 0.27], [3.3 eV, 6.8 eV] and [8.55 eV, 10.6 eV]. We can conclude that over these intervals, the material behaves like a metal and reflects external waves.

The imaginary part is also divided into the same three regions as the real part, namely: from 0 to 5 eV, where it is high; from 5 eV to 10 eV, where it takes on rather low values; and finally from 10 eV to 20 eV, where it is zero. In a solid material, the imaginary (absorbing) part $\varepsilon_2(\omega)$ of the dielectric function is strongly linked to the electronic band structure. The perovskite CH3NH3SiCl3 exhibits several peaks due to electronic transitions. The most significant are: 22.36 at 0.04 eV; 9.93 at 0.6 eV; 11.69 at 1.39 eV; 14.17 at 1.80 eV; 7.94 at 2.12 eV; 11.69 at 3.13 eV; 13.47 at 3.44 eV, 1.28 at 5.34 eV and 5.42 at 8.58 eV for $LiSiI_3$, $NaSiI_3$, $KSiI_3$, $RbSiI_3$ and $CsSiI_3$ respectively.

Now, let us examine the various optical functions and then confirm this analysis

### 3.3.2. Optical fonctions

Other optical properties, such as the refractive index $n(\omega)$, extinction coefficient $k(\omega)$, reflectivity $R(\omega)$, absorption coefficient $\alpha(\omega)$, optical conductivity $\sigma(\omega)$ and others, can be derived from $\varepsilon_r(\omega)$ and $\varepsilon_i(\omega)$.

$$n(\omega) = \left[\frac{\varepsilon_r(\omega)}{2} + \frac{\sqrt{\varepsilon_r{}^2(\omega) + \varepsilon_i{}^2(\omega)}}{2}\right]^{\frac{1}{2}} \#(14)$$

$$k(\omega) = \left[-\frac{\varepsilon_r(\omega)}{2} + \frac{\sqrt{\varepsilon_r{}^2(\omega) + \varepsilon_i{}^2(\omega)}}{2}\right]^{\frac{1}{2}} \#(15)$$

$$R(\omega) = \frac{(n-1)^2 + k^2}{(n+1)^2 + k^2} \quad \text{or} \quad R\left[\frac{\sqrt{\varepsilon(\omega)} - 1}{\sqrt{\varepsilon(\omega)} + 1}\right]^2 \#(16)$$

$$\alpha(\omega) = \left[\frac{\varepsilon_r(\omega)}{2} + \frac{\sqrt{\varepsilon_r{}^2(\omega) + \varepsilon_i{}^2(\omega)}}{2}\right]^{\frac{1}{2}} \#(17)$$

$$\sigma(\omega) = \left[\frac{\varepsilon_r(\omega)}{2} + \frac{\sqrt{\varepsilon_r{}^2(\omega) + \varepsilon_i{}^2(\omega)}}{2}\right]^{\frac{1}{2}} \#(18)$$

$$I(\omega) = \sqrt{2}\omega\left[\sqrt{\varepsilon_r{}^2(\omega) + \varepsilon_i{}^2(\omega)} - \varepsilon_r(\omega)\right]^{\frac{1}{2}} \#(19)$$

$$L(\omega) = \mathrm{Im}\left[-\frac{1}{\tilde{\varepsilon}(\omega)}\right] = \frac{\varepsilon_r(\omega)}{\varepsilon_r{}^2(\omega) + \varepsilon_i{}^2(\omega)} \#(20)$$

$n(\omega)$, $k(\omega)$, $R(\omega)$, $\alpha(\omega)$, $\sigma(\omega)$and$L(\omega)$are illustrated by the figures10, 11, 12, 13, 14 et 15.

UNDER PEER REVIEW IN IJAR

**Refractive index**n(ω).

To predict the behaviour of photons in a medium as they propagate through it, we use the complex refractive index, which describes how photons affect the medium through which they propagate [31, 32]. The real part is the real refractive index n(ω). A high value of the refractive index n(ω) means that light propagates slowly through the medium in question; the light will therefore be deflected. Figure 11 shows the real refractive index.

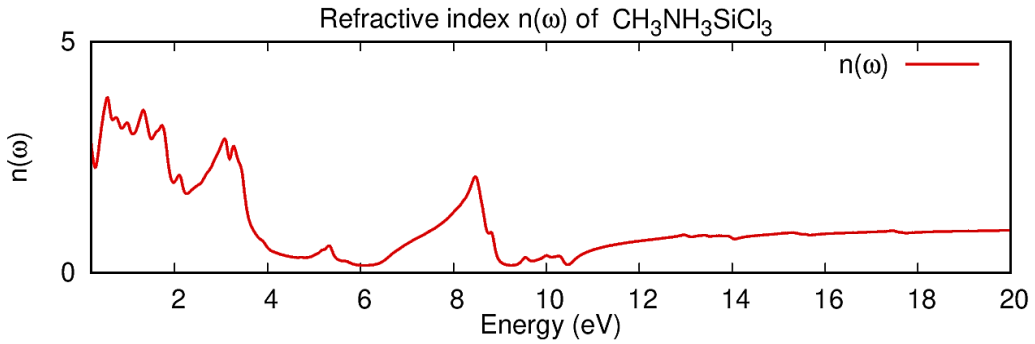



Figure 11 : Refractive index for $CH_3NH_3SiCl_3$.

The refractive index of the compound under study is positive and non-zero. In the energy ranges [0 eV; 3.65 eV] and [7.75 eV; 8.70 eV], it is greater than 1, so light travels more slowly in this medium than in a vacuum. [0 eV; 3.65 eV] corresponds to the infrared and visible spectrum, and [7.75 eV; 8.70 eV] to the ultraviolet spectrum. The static refractive index n(0) is 2.5. Lhouceine Moulaoui et al. obtained static refractive indices n(0) of 2.21 and 9.48 for $CH_3NH_3PbBr_3$ and $CH_3NH_3PbCl_3$ respectively [20]. The refractive index is greater than 2 from 0 eV to 3.5 eV and less than 1 for the energy intervals [3.65 eV; 7.75 eV] and [8.70 eV; 20 eV]. A peak at 8.5 eV, in the ultraviolet, is discernible. As this energy is very high, there is no photon–vibration interaction within the lattice (phonons), but rather a direct photon–electron interaction. An interband transition occurs: from the valence band, an electron absorbs a photon at 8.5 eV and transitions into the conduction band.

**Extinction coefficient**k(ω).

The extinction coefficient k(ω) corresponds to the imaginary part of the complex refractive index. It characterises the attenuation of the amplitude of light energy as it propagates through a material, as well as the reduction in the incident wave. For k(ω) = 0, the medium is completely and utterly transparent and therefore there is no attenuation. For k(ω) > 0, the energy is absorbed by the medium. The consequence is that the wave is attenuated. Figure 12 shows the extinction coefficient of $CH_3NH_3SiCl_3$.

UNDER PEER REVIEW

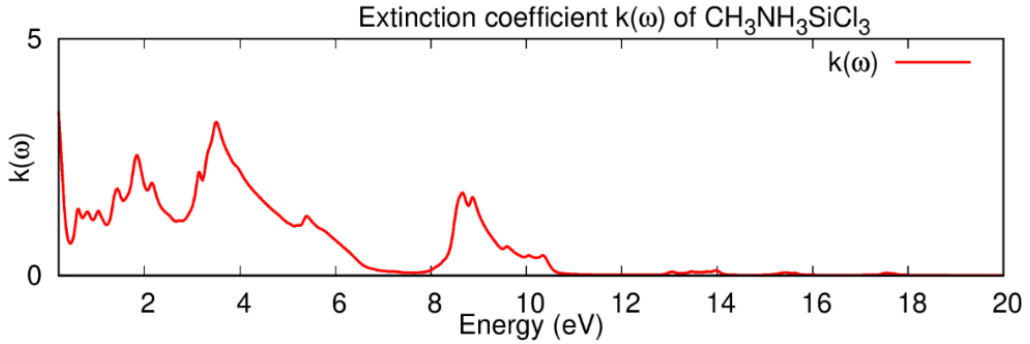



Figure 12 : Extinction coefficient for $CH_3NH_3SiCl_3$.

Four energy regions can be identified: [0 – 7 eV], [7 – 8 eV], [8 – 10.8 eV] and [10.8 – 20 eV]. k(ω) is zero over [7 – 8 eV] and [10.8 – 20 eV]. It follows that there is virtually no attenuation of the incident light in these energy regions. The medium is therefore transparent. Over [0 – 7 eV] and [8 – 10.8 eV], the incident light is attenuated because k(ω) > 0. The material therefore absorbs the light, resulting in a reduction in light intensity as it passes through the material..

**ReflexivityR(ω)**

When a light wave strikes a material, it may be reflected by that material. The optical reflectance R(ω) characterises this reflection. If R(ω) = 0, there is no reflection of the incident wave. In this case, it is either completely absorbed or transmitted. However, if R(ω) = 1, the incident wave is completely reflected. Figure 13 shows the optical reflectivity R(ω) of the perovskite material $CH_3NH_3SiCl_3$.

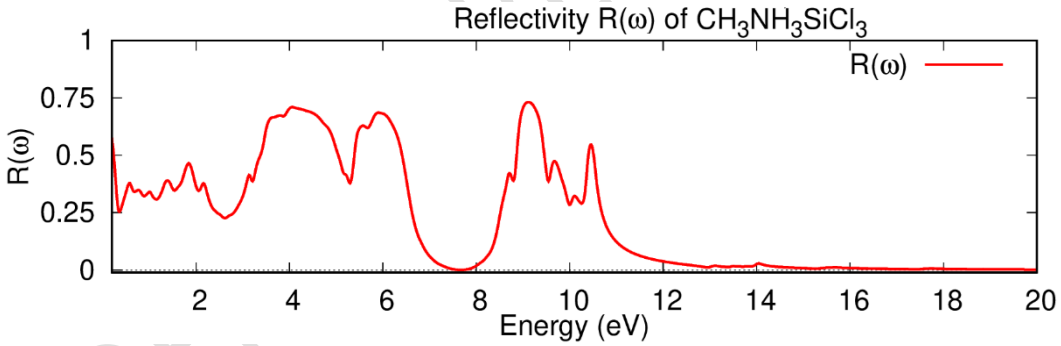



Figure 13 : Reflexivity of$CH_3NH_3SiCl_3$.

From 0 to 7.5 eV, the reflectivity is very high. It then drops to zero between 7.5 and 8 eV. It becomes high again between 8 eV and 13 eV, before falling to practically zero between 13 eV and 20 eV. We can therefore conclude that there are no reflected waves in the [7.5–8 eV] and [13–20 eV] ranges. However, a significant proportion is reflected in the [0–7.5 eV] and [8–13 eV] ranges.

**Absorption coefficient**

Figure 14 shows the absorption coefficient α(ω) of $CH_3NH_3SiCl_3$. The absorption coefficient α(ω) provides information on the penetration of light at a specific wavelength and energy prior to absorption. α(ω) indicates, at a specific frequency, the medium's ability to attenuate the incident light intensity as it travels through it. It also indicates the nature of the material. If α(ω) is high, light is

UNDER PEER REVIEW IN IJAR

strongly absorbed. Reflection occurs because transmission is low. If α(ω) is low, the material is highly transparent.

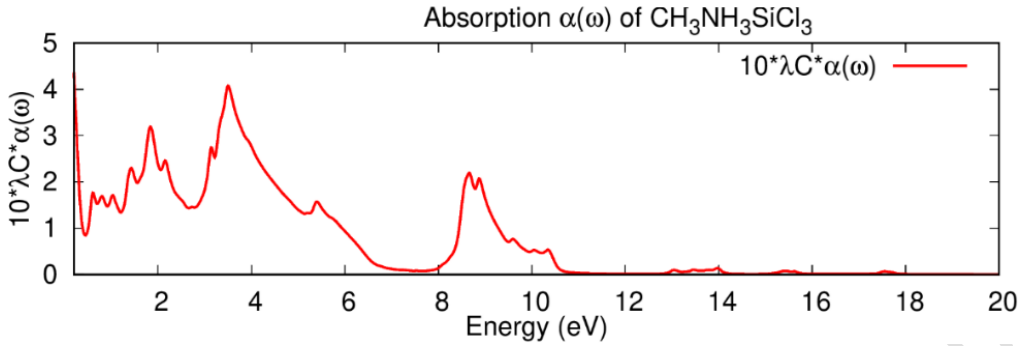



Figure 14: Absorption coefficient for $CH_3NH_3SiCl_3$.

The absorption curve is similar to that of the extinction curve. Absorption occurs from 0 eV to 7 eV and then from 8 eV to 10.50 eV. Absorption is zero between 7 eV and 8 eV and between 10.50 eV and 20 eV. From the above, it follows that absorption therefore occurs in the infrared and visible regions..

**Optical conductivity**

Optical conductivity σ(ω) explains the transport of electrons when matter interacts with light [20]. It describes how a material responds electrically to an electromagnetic wave oscillating at a certain frequency. σ(ω) also defines the relationship between the induced current density in the material and the amplitude of the inducing electric field [20]. Figure 16 shows the optical conductivity of $CH_3NH_3SiCl_3$.

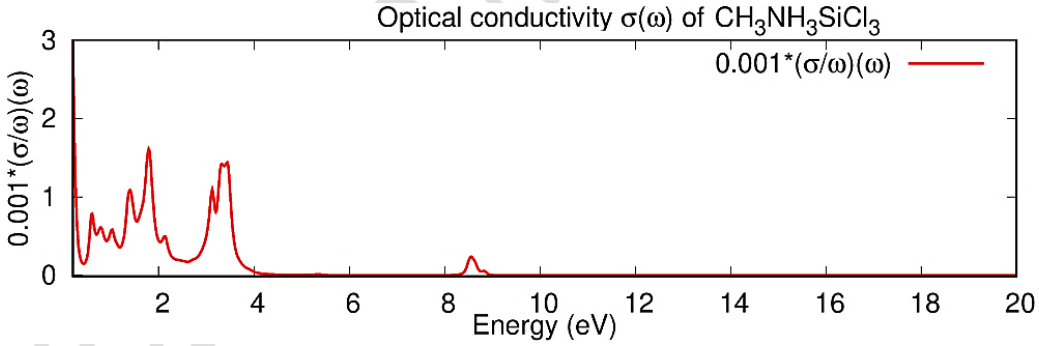



Figure 16 : Optical conductivity for $CH_3NH_3SiCl_3$.

$CH_3NH_3SiCl_3$ begins to conduct from 0 eV up to 3.95 eV. σ(ω) is zero up to 8.3 eV. From 8.3 eV to 8.8 eV, σ(ω) is rather weak, then becomes zero after 8.8 eV. It is strong from 0 eV to 3.95 eV and weak from 3.95 eV to 10 eV. There is therefore light-matter interaction with the material from 0 eV to 3.95 eV, and consequently electron transport at these energies. The energy region from 8.3 eV to 8.8 eV corroborates the observation made for the real refractive index. This is because a peak was observed around 8.5 eV. This therefore explains the low optical conductivity in the ultraviolet. There is direct photon–electron interaction. The static conductivity σ(0) is $3.06 \times 10^5 \mathrm{cm}^{-1}$.

**Energy loss function**

UNDER PEER REVIEW IN IJAR

The electron energy loss function L(ω) characterises the optical energy loss caused by scattering or by the heating of electrons propagating through a medium [19]. It quantifies how the medium absorbs the energy supplied by an external light wave or by an external electron beam [33]. Figure 17 shows the energy loss spectrum of $CH_3NH_3SiCl_3$. From 0 to 50 eV, the L(ω) spectrum corresponds to the valence loss spectrum. This energy region corresponds to the dielectric response at a frequency of $10^{15}$ Hz (or from 10 eV to 20 eV), in which the valence electrons cause resonant oscillations.

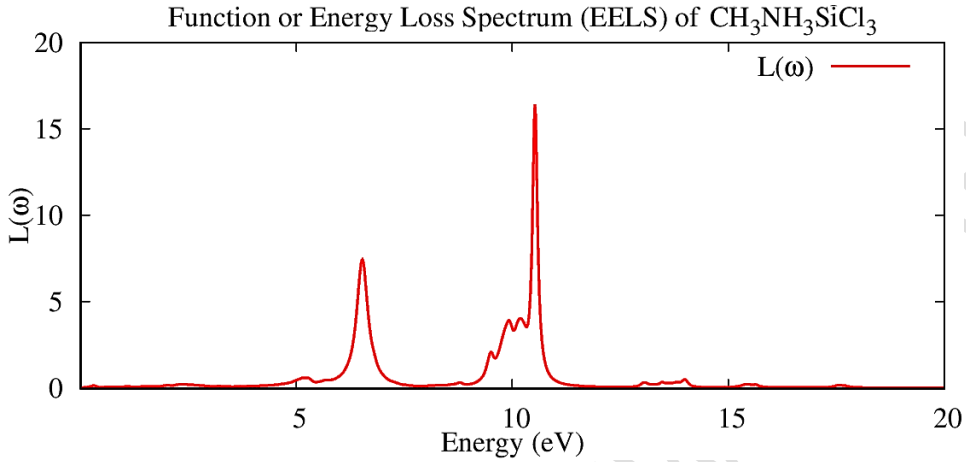



Figure 17. Energy loss function spectrum of $CH_3NH_3SiCl_3$.

This indicates that $CH_3NH_3SiCl_3$ is a low-energy conductive material. It certainly has a high photoelectric conversion efficiency (PCE). This was also the finding for $MAPbCl_3$ studied by Lhouceine Moulaoui et al [20]. The electron energy loss graph L(ω) shows a major peak with a maximum value ranging from 16.41 to 10.521 eV. This means that the medium is excited due to a loss of photon energy upon interaction with the material. This peak, at its maximum, corresponds to the material's plasma frequency. At this maximum peak, the electrons begin to vibrate in unison under the influence of light. In turn, this accumulation of electrons acts as a barrier and weakens the initial light signal. A first peak is also observed, though less intense than the previous one: a peak of 6.53 at 7.42 eV..

## CONCLUSION

This study enabled us to determine the structural, electronic and optical properties of the perovskite material $CH_3NH_3SiCl_3$ using the DFT method and the GGA formalism. The perovskite $CH_3NH_3SiCl_3$ was modelled as a Pm-3m cubic structure. The lattice parameter of $CH_3NH_3SiCl_3$ was found to be 5.72 Å. The bandgap energy was found to be 2.509 eV along the R-R path. $CH_3NH_3SiCl_3$ is therefore a semiconductor. Analysis of the density of states (DOS) and partial densities of states (PDOS) shows that the valence band is characterised by the 2p-Cl state, which is weakly mixed with the 2p-C, 2p-Si and 2p-N states. The conduction band is predominantly influenced by the 2p-Si state. With regard to optical properties, over [0 eV; 3.65 eV] and [7.75 eV; 8.70 eV], the refractive index is greater than 1, indicating that light propagates more slowly in this medium than in a vacuum, and is susceptible to deviation in the IR, visible and UV regions. The medium is also transparent over [7–8 eV] and [10.8–20 eV]. For [0–7 eV] and [8–10.8 eV], the intensity of incident light is attenuated as it passes through

UNDER PEER REVIEW IR

the material. The reflectance data show that light can be reflected in the ranges from 0 to 7.5 eV and from 8 eV to 13 eV.Absorption occurs in both the infrared and visible regions. The optical conductivity shows that the material begins to conduct between 0 eV and 3.95 eV, but this conductivity decreases between 8.3 eV and 8.8 eV. The conductivity is therefore higher in the IR than in the UV. There is no interaction between photons and lattice vibrations (phonons), but rather a direct interaction between photons and electrons. $CH_3NH_3SiCl_3$ is a low-energy conductor. It certainly has a high photoelectric conversion efficiency (PCE). The photon energy loss function reveals a maximum peak at 7.421 eV. At this maximum peak, the electrons begin to vibrate collectively under the effect of light. In turn, this accumulation of electrons acts as a barrier and weakens the initial light signal. A first peak, though less intense than the previous one, is observed between 6.529 and 7.421 eV.The $CH_3NH_3SiCl_3$ perovskite studied possesses highly interesting electronic, optoelectronic and optical properties. It could be used in photovoltaic cells and other electronic devices. It is an ideal candidate for the manufacture of UV absorbers and detectors. This material can be incorporated into devices that are essential to current technologies.

**REMERCIEMENTS**

We would like to express our thanks to the Physics Department at Jean Lorougnon Guede University (UJLoG) in Daloa (Daloa, Côte d'Ivoire), the Laboratory of Environmental Science and Technology (LSTE) at UJLoG (Daloa, Côte d'Ivoire), the Laboratory of Fundamental and Applied Physics (LPFA) at NANGUI ABROGOUA University (Abidjan, Côte d'Ivoire) and the Laboratory of Information and Communication Science and Technology (LASTIC), ESATIC, Abidjan, Côte d'Ivoire, for their collaboration on this study. Both teams contributed significantly to the completion of this work.

**REFERENCES**

[1] Al Mubarak, F., Rezaee, R., & Wood, D. A. (2024). *Economic, Societal, and Environmental Impacts of Available Energy Sources: A Review*. Engineering, 5(3), 1232–1265. 10.3390/eng5030067

[2] Pabitra K. Nayak, Suhas Mahesh, Henry J. Snaith & David Cahen. Photovoltaic solar cell technologies: analysing the state of the art. Nature Reviews Materials volume 4, pages269–285 (2019).

[3] Sharma, P., & Mishra, R. K. (2025). Comprehensive study on photovoltaic cell's generation and factors affecting its performance: A review. *Materials for Renewable and Sustainable Energy, 14*, Article 21. DOI : https://doi.org/10.1007/s40243-024-00292-5

[4] Urbina, A. (2023). Sustainability of photovoltaic technologies in future net-zero emissions scenarios. *Progress in Photovoltaics: Research and Applications, 31*(12), 1255–1269. DOI : https://doi.org/10.1002/pip.3642

[5] Masson, G., de l'Epine, M., & Kaizuka, I. (2024). *Trends in photovoltaic applications 2024*. International Energy Agency Photovoltaic Power Systems Programme (IEA PVPS), Report IEA PVPS T1-43:2024.

UNDER PEER REVIEW IN IJAR

[6] Ahn, N., Son, D.-Y., Jang, I.-H., Kang, S. M., Choi, M., & Park, N.-G. (2015). Highly reproducible perovskite solar cells with average efficiency of 18.3% and best efficiency of 19.7% fabricated via Lewis base adduct of lead(II) iodide. Journal of the American Chemical Society, 137(27), 8696–8699. DOI : https://doi.org/10.1021/jacs.5b04930

[7] Green, M. A., Emery, K., Hishikawa, Y., Warta, W., & Dunlop, E. D. (2015). Solar cell efficiency tables (Version 45). Progress in Photovoltaics: Research and Applications, 23(1), 1–9. DOI : https://doi.org/10.1002/pip.2573

[8] Faini, F., Larini, V., Scardina, A., et al. (2024). Hybrid halide perovskites, a game changer for future solar energy? MRS Bulletin, 49, 1059–1069. DOI : https://doi.org/10.1557/s43577-024-00784-9

[9] Dastgeer, G., Nisar, S., Zulfiqar, M. W., Eom, J., Imran, M., & Akbar, K. (2024). A review on recent progress and challenges in high-efficiency perovskite solar cells. Nano Energy, 132, Article 110401. DOI : https://doi.org/10.1016/j.nanoen.2024.110401

[10] Miah, M. H., Khandaker, M. U., Rahman, M. B., Nur-E-Alam, M., & Islam, M. A. (2024). Band gap tuning of perovskite solar cells for enhancing the efficiency and stability: Issues and prospects. RSC Advances, 14, 15876–15906. DOI : https://doi.org/10.1039/D4RA01640H

[11] Wang, et al. (2023). Advances in the application of perovskite materials. Nano-Micro Letters, 15, Article 177. DOI : https://doi.org/10.1007/s40820-023-01140-3

[12] Khorasani, A. (2024). Opportunities, challenges, and strategies for scalable deposition of metal halide perovskite solar cells and modules. Advanced Energy and Sustainability Research. DOI : https://doi.org/10.1002/aesr.202300275

[13] Hu, C., Li, B., Wang, X., Liu, C., Sun, D., et al. (2025). Recent progress in the patterning of perovskite films for photodetector applications. Light: Science & Applications, 14, Article 355. DOI : https://doi.org/10.1038/s41377-025-01958-z

[14] Xu, J., Wu, Y., Fan, S., Liu, X., Yin, Z., Yang, Y., Wang, R., Qian, Z., & Sun, Y. (2024). Real-time detection of aging status of methylammonium lead iodide perovskite thin films by using terahertz time-domain spectroscopy. Frontiers of Optoelectronics, 17, Article 24. https://doi.org/10.1007/s12200-024-00128-0.

[15] Davies, C. L., Filip, M. R., Patel, J. B., Crothers, T. W., Verdi, C., Wright, A. D., Milot, R. L., Giustino, F., Johnston, M. B., & Herz, L. M. (2018). Bimolecular recombination in methylammonium lead triiodide perovskite is an inverse absorption process. Nature Communications, 9, Article 293. https://doi.org/10.1038/s41467-017-02670-2.

[16] Kojima, A., Teshima, K., Shirai, Y., & Miyasaka, T. (2009). Organometal halide perovskites as visible-light sensitizers for photovoltaic cells. Journal of the American Chemical Society, 131(17), 6050–6051. https://doi.org/10.1021/ja809598r

[17] Ge, Y., Wang, H., Wang, C., Wang, C., Guan, H., Shao, W., Wang, T., Ke, W., Tao, C., & Fang, G. (2023). Intermediate phase engineering with 2,2-azodi(2-methylbutyronitrile) for efficient and stable perovskite solar cells. *Advanced Materials*, *35*(23), Article 2210186. https://doi.org/10.1002/adma.202210186

UNDER PEER REVIEW IN IJAR

[18] Sha, W. E. I., Ren, X., Chen, L., & Choy, W. C. H. (2015). The efficiency limit of $CH_3NH_3PbI_3$ perovskite solar cells. Applied Physics Letters, 106(22), Article 221104. https://doi.org/10.1063/1.4922150.

[19] R. Garnier, Toxicité du plomb et de ses dérivés (Toxicity of lead and its derivatives), EMC - Toxicol.-Pathol. (2005) https://doi.org/10.1016/j.emctp.2004.10.004

[20] Lhouceine Moulaoui*, Omar Bajjou, Abdelhafid Najim and Khalid Rahmani. The study of electronic and optical properties of perovskites $CH3NH3PbCl_3$ and $CH3NH3PbBr_3$ using first-principle. E3S Web of Conferences 336, 00015 (2022).

[21] Grover, K., Choudhary, J. S., Bhardwaj, S., Muduli, P. K., Kumar, P., Hmar, J. J. L., Jha, R., & Yadav, H. (2026). A systematic facet-specific mechanical, photodetection, and DFT analysis of $MAPbCl_3$ perovskite single crystals. Materials Science in Semiconductor Processing, 208, Article 110562. https://doi.org/10.1016/j.mssp.2026.110562

[22] P Giannozzi, S Baroni, N Bonini, M Calandra, R Car, C Cavazzoni, D Ceresoli, G L Chiarotti, M Cococcioni, I Dabo, A Dal Corso, S Fabris, G Fratesi, S de Gironcoli, R Gebauer, U Gerstmann, C Gougoussis, A Kokalj, M Lazzeri, L Martin-Samos, N Marzari, F Mauri, R Mazzarello, S Paolini, A Pasquarello, L Paulatto, C Sbraccia, S Scandolo, G Sclauzero, A P Seitsonen, A Smogunov, P Umari, and R M Wentzcovitch. QUANTUM ESPRESSO: a modular and open-source software project for quantum simulations of materials. Journal of Physics: Condensed Matter. (2009), 21(39), p. 395502.

[23] P. Giannozzi, O. Andreussi, T. Brumme, O. Bunau, M. Buongiorno Nardelli, M. Calandra, R. Car, C. Cavazzoni, D. Ceresoli, M. Cococcioni, N. Colonna, I. Carn imeo, A. Dal Corso, S. de Gironcoli, P. Delugas, R. A. DiStasio Jr, A. Ferretti, A. Floris, G. Fratesi, G. Fugallo, R. Gebauer, U. Gerstmann, F. Giustino, T. Gorni, J Jia, M. Kawamura, H.-Y. Ko, A. Kokalj, E. K¨u¸c¨ukbenli, M .Lazzeri, M. Marsili, N. Marzari, F. Mauri, N. L. Nguyen, H.-V. Nguyen, A. Otero-de-la-Roza, L. Paulatto, S. Ponc´e, D. Rocca, R. Sabatini, B. Santra, M. Schlipf, A. P. Seitsonen, A. Smo gunov, I. Timrov, T. Thonhauser, P. Umari, N. Vast, X. Wu, S. Baroni, J.Phys.: "Advancd capabilities for materials modelling with Quantum ESPRESSO". Condens.Matter 29, 465901 (2017).

[24] P. Giannozzi, O. Baseggio, P. Bonf`a, D. Brunato, R. Car, I. Carnimeo, C. Cavazzoni, S. de Gironcoli, P. Delugas, F. Ferrari Ruffino, A. Ferretti, N. Marzari, I. Timrov, A. Urru, S. Baroni, J. Chem. Phys. 152, 154105 (2020)

[25] J P Perdew, K Burke & M Ernzerhof. Generalized Gradient Approximation Made Simple. [Phys. Rev. Lett. 77, 3865 (1996)]. In: Physical Review Letters, (1997), 78(7), p. 1396-1396.

[26] A D Becke. Density-functional exchange-energy approximation with correct asymptotic behavior. In: Physical Review A, (1988), 38(6), p. 3098–3100.

[27] Morgan, W. S., Christensen, J. E., Hamilton, P. K., Jorgensen, J. J., Campbell, B. J., Hart, G. L. W., & Forcade, R. W. (2020). Generalized regular k-point grid generation on the fly. Computational Materials Science, 173, 109340. DOI : https://doi.org/10.1016/j.commatsci.2019.109340

[28] Martin, R. M. (2004). Electronic Structure: Basic Theory and Practical Methods. Cambridge University Press. DOI : https://doi.org/10.1017/CBO9780511805769

UNDER PEER REVIEW IN JAP

[29] Marder, M. P. (2010). Condensed Matter Physics (2nd ed.). John Wiley & Sons. DOI : https://doi.org/10.1002/9780470949955

[30] Kolomiiets, V., Kapustianyk, V., Kovalenko, M., Kraus, H., Chukova, O., Zhydachevskyy, Y., Zia, W., Saliba, M., & Mykhaylyk, V. (2025). Electronic structure, reflectivity and X-ray luminescence of $MAPbCl_3$ crystal in orthorhombic phase. Scientific Reports, 15, Article 12912. https://doi.org/10.1038/s41598-025-96694-0.

[31] Sasaki, S. (2022). Determination of complex refractive index using prism composed of absorbing medium. Results in Optics, 8, 100260. DOI : https://doi.org/10.1016/j.rio.2022.100260

[32] Perea-Puente, S., & Rodríguez-Fortuño, F. J. (2024). Complex Refraction Metasurfaces for Locally Enhanced Propagation Through Opaque Media. Laser & Photonics Reviews, 18(5), 2300867. DOI : https://doi.org/10.1002/lpor.202300867

[33] M. Ashiq, Q. Mahmood, T. Zelai, O. Hakami, N. A. Kattan, H. Albalawi, A. Aljameel, S. Bouzgarrou, T. Ghrib, K. I. Hussein, The narrow band bap double perovskites x2cuincl6 (x = k, rb, cs) for optoelectronics, and thermoelectric applications, Materials Science and Engineering: B 296 (2023) 116690.

UNDER PEER REVIEW IN IJAR